RSC Advances

PAPER

View Article Online
View Journal | View Issue

Cite this: *RSC Adv.*, 2021, **11**, 16359

UV-visible light-induced photochemical synthesis of benzimidazoles by coomassie brilliant blue coated on W–ZnO@NH$_2$ nanoparticles

Ruijuan Chen,[a] Zahra Jalili *[b] and Reza Tayebee *[b]

Received 26th December 2020
Accepted 17th April 2021

DOI: 10.1039/d0ra10843j

rsc.li/rsc-advances

Heterogeneous photocatalysts proffer a promising method to actualize eco-friendly and green organic transformations. Herein, a new photochemical-based methodology is disclosed in the preparation of a wide range of benzimidazoles through condensation of *o*-phenylenediamine with benzyl alcohols in the air under the illumination of an HP mercury lamp in the absence of any oxidizing species catalyzed by a new photocatalyst W–ZnO@NH$_2$–CBB. In this photocatalyst, coomassie brilliant blue (CBB) is heterogenized onto W–ZnO@NH$_2$ to improve the surface characteristics at the molecular level and enhance the photocatalytic activity of both W–ZnO@NH$_2$ and CBB fragments. This unprecedented heterogeneous nanocatalyst is also identified by means of XRD, FT-IR, EDS, TGA-DTG, and SEM. The impact of some influencing parameters on the synthesis route and effects on the catalytic efficacy of W–ZnO@NH$_2$–CBB are also assessed. The appropriate products are attained for both the electron-withdrawing and electron-donating substituents in the utilized aromatic alcohols. Furthermore, preparation of benzimidazoles is demonstrated to occur mainly *via* a radical mechanism, which shows that reactive species such as $\cdot O_2^-$, OH$^{\cdot}$ and h$^+$ would be involved in the photocatalytic process. Stability and reusability studies also warrant good reproducibility of the nanophotocatalyst for at least five runs. Eventually, a hot filtration test proved that the nanohybrid photocatalyst is stable in the reaction medium. Using an inexpensive catalyst, UV-vis light energy and air, as a low cost and plentiful oxidant, puts this methodology in the green chemistry domain and energy-saving organic synthesis strategies. Finally, the anticancer activity of W–ZnO nanoparticles is investigated on MCF7 breast cancer cells by MTT assay. This experiment reveals that the mentioned nanoparticles have significant cytotoxicity towards the selected cell line.

1 Introduction

These days, choosing a suitable energy source for research projects is one of the significant topics of interest to the scientific community. This important challenge has led scientists to pay close attention to the main features of an acceptable energy source comprising cheapness, renewability, environmental friendliness, availability, sustainability and more. The sun as one of the infinite, clean and affordable energy sources can be chosen as an appropriate option for energy usage.[1] Observing the behavior of nature in the use of solar energy to produce carbohydrates and oxygen in the biochemical processes based on oxidation–reduction reactions, leads scientists to understand that they are able to use this energy as a catalyst activator in many chemical reactions such as water-splitting reactions,[2] degradation of organic pollutants,[3] polymerization,[4] organic synthesis[5] and semiconductor chemistry.[6]

Amongst hetero-containing double-ring aromatic compounds, benzimidazoles are highly regarded because they are widely used in the field of agriculture,[7] parasitic infections,[8] anti-corrosion[9] and antioxidant industries.[10] Various pharmaceutical properties of these compounds are also studied in the vast majority of areas such as antimicrobial,[11] antiviral,[12] anticancer,[13] antiprotozoal,[14] antitubercular,[15] anti-inflammatory[16] and anti-analgesic.[17] Because of the wide range of benzimidazoles' applications, the preparation of these critical compounds has received special consideration in the past two decades. Expanding simple and ecological trends or techniques to extensively attain organic materials from easily accessible chemicals is another main subject in the chemical communities. There are several common procedures for the synthesis of benzimidazoles and 2-substituted benzimidazoles from the reaction of *o*-phenylenediamine with different reagents, such as aromatic aldehydes,[18] acid anhydrides,[19] amides, acid chlorides,[20] esters and nitriles.[21] Although preparation of benzimidazoles *via* the *in situ* oxidation of benzylic alcohols in the

---

[a] *Department of Obstetrics and Gynecology, Xi'an Central Hospital, Xi'an, 710000, China*

[b] *Department of Chemistry, School of Sciences, Hakim Sabzevari University, Sabzevar, 96179-76487, Iran. E-mail: m.jalili2011@yahoo.com; rtayebee@hsu.ac.ir*

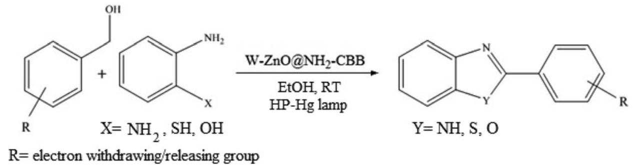

Scheme 1 The schematic diagram for the synthesis of benzimidazoles in the presence of W–ZnO@NH$_2$–CBB nanophotocatalyst.

presence of diamines is previously reported, however, these methods suffer from some significant drawbacks such as lengthy reaction time, usage of O_2 as oxidant, production of stoichiometric quantities of wastes, using toxic reagents, poor yield, toxic solvents, and so on.[22,23] Nowadays, seeking synthetic routes to prepare benzimidazoles under greener conditions is of great importance because of the wide application of these compounds in life.

The other important and common factor in all methods disclosed for the preparation of benzimidazoles is due to the existence of a suitable catalyst. So far, various catalysts have been used to synthesize these compounds such as magnetic catalysts,[24] porous materials,[25] metal–organic frameworks,[26] ionic liquids,[27] heavy metal oxides,[28] graphene oxide[29] and so on. By consideration of all the existing literature, we wish to disclose a new heterogeneous photocatalyst in the preparation of 2-substituted benzimidazoles by the reaction of some substituted *o*-substituted anilines with benzyl alcohols in the presence of air, as the source of oxidizing agent, under the photocatalytic conditions (Scheme 1). The impact of solvent, temperature, and source of the illumination are investigated here. Further, different electron-donating/withdrawing substituents on the phenyl ring of benzyl alcohol as well as some substituted anilines are also tested in this report. In addition, some familiar radical and hole scavengers are studied in the present protocol to confirm that the reactive species such as $\cdot O_2^-$, $OH^\bullet$ and h^+ are responsible to the present photocatalytic process. Stability and reusability studies are also investigated *via* hot filtration test to warranty reproducibility of the photocatalytic route.

2 Experimental

2.1 Materials and methods

All chemicals were purchased from Sigma-Aldrich, Fluka and Merck and applied as received without any further purification. A high-pressure mercury lamp (400 W, NARVA, Berlin) with a nominal voltage of 230 V, lamp-operating current 3.25 A and optical power of 80 W was applied for the photocatalytic tests. A Mira 3-MU field emission scanning electron microscopy (FESEM) was used to investigate morphology of the synthesized nanomaterial. FT-IR spectra were recorded with KBr pellets at room temperature at the range of 400–4000 cm^{-1} using a Shimadzu 8700 Fourier transform spectrophotometer. ^{1}H- and ^{13}C-NMR spectra were recorded on a 300 MHz Bruker AVANCEC III spectrometer in DMSO-d^6 using TMS as the internal reference. A DMAX-2500, Rigaku X-ray diffractometer (with Cu Kα radiation in the 2θ domain at 30 mA and 40 keV with the scanning rate of 3° min^{-1} from 5° to 80°) was used to obtain the X-ray diffraction (XRD) patterns. Thermogravimetric analysis was carried out by a TGA 92 Setaram at 10 °C min^{-1}. UV-visible spectra were recorded with a Photonix UV-visible array spectrophotometer. The surface area and pore distribution of nanocomposite were determined by a BET surface area analyzer (Belsorp mini2, Japan).

2.2 Synthesis of photocatalyst

2.2.1 Preparation of W–ZnO nanoparticles. W–ZnO was synthesized *via* a modified method.[30] 35 mL NaOH (4 M) was added drop-wise into a mixture of sodium tungstate (2.5 mL, 0.5 M) and zinc acetate dihydrate (22 mL, 1 M) in water. The obtained suspension was stirred at room temperature to form the precursor and after 3 h, the suspension was delivered to a 250 mL ground-glass stopped conical flask, diluted with deionized water up to the mark-line and heated for 10 h at 95 °C. The produced precipitate was gathered, washed with deionized water and dried at ambient temperature in air.

2.2.2 Functionalization of W–ZnO nanoparticles with 3-(triethoxysilyl)propylamine (W–ZnO@NH$_2$). At first, 0.85 g of W–ZnO nanoparticles well dispersed in 60 mL anhydrous toluene under ultrasonic. Then, the mixture was refluxed for 24 h after addition of 1.6 mL 3-(triethoxysilyl)propylamine. Finally, the deposited precipitate was collected and dried in an oven at 60 °C for 12 h.

2.2.3 Functionalization of W–ZnO@NH$_2$ nanoparticles with various photosensitizers. The well-known wet impregnation strategy was used to synthesize W–ZnO@NH$_2$– (photosensitizer) nanoparticles. Therefore, a general route is demonstrated for all photosensitizers as follows. At first, 0.02 g of each photosensitizer was dissolved in THF (20 mL), then, 0.5 g of WZnO–NH$_2$ nanoparticles was gradually added to this solution during 12 h in a dark place. Eventually, the obtained precipitate was dried at 80 °C for 24 h under air. All photosensitizers in Fig. 8a were functionalized with this method on WZnO–NH$_2$ nanoparticles.

2.3 A general route for the synthesis of benzimidazoles from benzyl alcohols and *o*-phenylenediamines

A mixture of W–ZnO@NH$_2$–CBB nanocomposite (0.02 g) as photcatalyst, benzyl alcohol (1.0 mmol) and *o*-phenylenediamine (1.2 mmol) in ethanol (10 mL) was stirred at room temperature. Thereafter, the reaction mixture was exposed to the HP mercury light under mild air bubbling (1 mL min^{-1}) with stirring and progress of the reaction followed by TLC. After completion, the nanophotocatalyst was separated from the reaction mixture and the yellow product was attained after addition of ice water. The precipitated product was recrystallized in ethanol to provide the pure product.

2.4 Spectral NMR data of the prepared benzimidazoles, benzothiazoles and benzoxazoles

Table 3, entry 1. ^{1}H NMR (300 MHz, DMSO-d$_6$); δ 7.19–7.22 (m, 3H), 7.57–7.60 (m, 2H), 7.64–7.67 (m, 2H), 8.19–8.21 (d, 2H), 13.07 (brs, 1H, NH) ppm; ^{13}C NMR (75 MHz, DMSO-d$_6$);

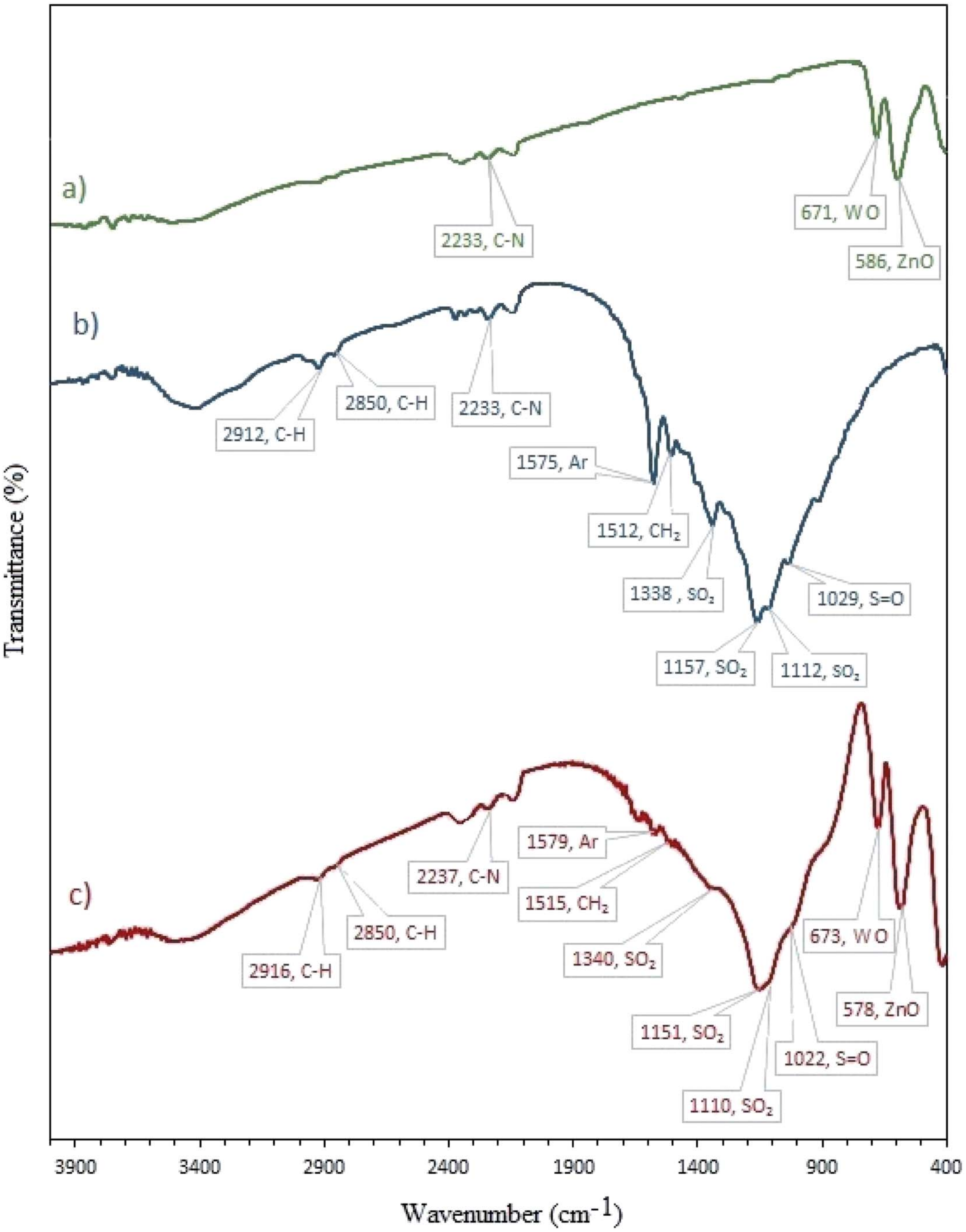

Fig. 1 FT-IR spectra of (a) W–ZnO@NH$_2$, (b) CBB and (c) W–ZnO@NH$_2$–CBB.

δ 115.62, 122.64, 126.63, 127.05, 129.39, 129.54, 129.59, 130.45, 137.42, 143.14, 151.83 ppm.

Table 3, entry 2. ^{1}H NMR (300 MHz, DMSO-d$_6$); δ 2.36 (s, 3H), 7.18–7.21 (m, 2H), 7.35–7.37 (d, 2H), 7.60–7.69 (m, 2H), 8.11–8.14 (d, 2H), 12.79 (s, 1H, NH) ppm; ^{13}C NMR (75 MHz, DMSO-d$_6$); δ 21.37, 111.49, 119.26, 122.12, 122.83, 126.93, 128.04, 130.07, 135.62, 140.31, 144.41, 151.98 ppm.

Table 3, entry 3. ^{1}H NMR (300 MHz, DMSO-d$_6$); δ 7.21–7.24 (m, 2H), 7.49–7.55 (m, 2H), 7.67–7.70 (m, 2H), 8.23–8.27 (d, 1H), 8.39 (s, 1H), 13.21 (brs, 1H, NH) ppm; ^{13}C NMR (75 MHz, DMSO-d$_6$); δ 112.16, 119.71, 122.69, 122.92, 123.57, 123.88, 126.05, 129.56, 131.83, 133.04, 135.67, 144.70, 150.63 ppm.

Table 3, entry 4. ^{1}H NMR (300 MHz, DMSO-d$_6$); δ 7.24–7.28 (m, 2H), 7.59–7.69 (m, 4H), 8.20–8.23 (m, 1H), 8.25–8.29 (m, 1H), 12.81 (brs, 1H, NH) ppm; ^{13}C NMR (75 MHz, DMSO-d$_6$); δ 112.12, 119.71, 122.63, 123.47, 123.98, 129.13, 130.21, 132.84, 135.94, 145.03, 151.16 ppm.

Table 3, entry 5. ^{1}H NMR (300 MHz, DMSO-d$_6$); δ 7.35–7.37 (m, 2H), 7.41–7.44 (m, 2H), 7.49–7.52 (m, 1H), 7.74–7.76 (m, 2H), 8.45–8.47 (m, 1H), 10.51 (brs, 1H, NH) ppm. ^{13}C NMR (75

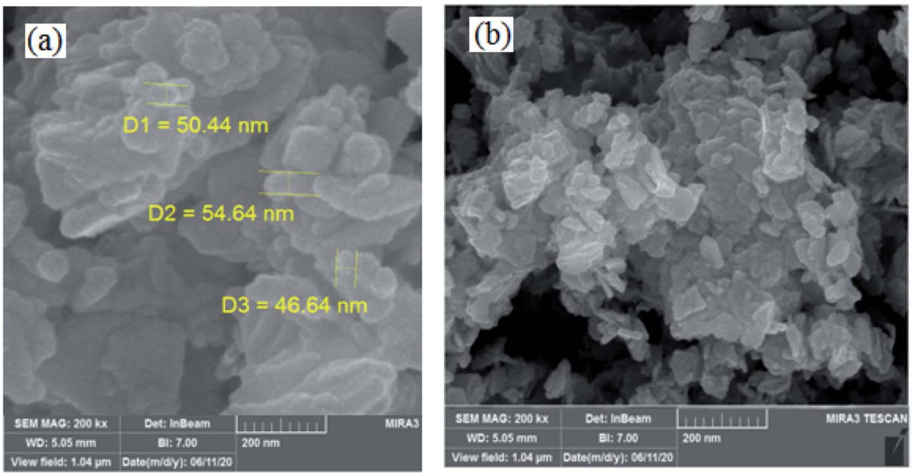

Fig. 2 FESEM images of (a) W–ZnO@NH_2 and (b) W–ZnO@NH_2–CBB.

MHz, DMSO-d_6); δ 123.11, 127.93, 130.16, 130.83, 131.46, 131.89, 132.57, 150.01 ppm.

Table 3, entry 6. ^{1}H NMR (300 MHz, DMSO-d_6); δ 7.22–7.25 (m, 2H), 7.60–7.62 (m, 2H), 7.63–7.66 (m, 1H), 7.70–7.72 (m, 1H), 8.21–8.23 (m, 1H), 8.27–8.29 (m, 1H), 13.21 (brs, 1H, NH) ppm; ^{13}C NMR (75 MHz, DMSO-d_6); δ 111.93, 119.61, 122.58, 123.42, 125.49, 126.55, 129.87, 131.60, 132.72, 134.34, 135.53, 144.67, 151.01 ppm.

Table 3, entry 7. ^{1}H NMR (300 MHz, DMSO-d_6); δ 7.24–7.30 (m, 2H), 7.56–7.59 (d, 2H), 7.67–7.72 (m, 3H), 8.21–8.25 (d, 2H), 13.05 (s, 1H, NH) ppm; ^{13}C NMR (75 MHz, DMSO-d_6); δ 112.08, 119.62, 122.73, 123.63, 128.99, 129.85, 129.67, 135.17, 135.79, 144.49, 150.96 ppm.

Table 3, entry 8. ^{1}H NMR (300 MHz, DMSO-d_6); δ 7.21–7.25 (m, 2H), 7.57–7.60 (m, 2H), 7.59–7.65 (m, 1H), 8.20–8.23 (m, 1H), 8.21–8.25 (m, 1H), 13.12 (brs, 1H, NH) ppm; ^{13}C NMR (75 MHz, DMSO-d_6); δ 112.31, 119.89, 122.38, 123.42, 128.99, 129.13, 131.53, 132.99, 134.73, 135.75, 143.79, 143.92, 147.54 ppm.

Table 3, entry 9. ^{1}H NMR (300 MHz, DMSO-d_6); δ 7.27–7.31 (m, 2H), 7.60–7.62 (m, 1H), 7.69–7.72 (m, 1H), 7.77–7.81 (m, 1H), 7.87–7.93 (t, 1H), 8.92–8.09 (m, 2H), 13.12 (s, 1H, NH) ppm; ^{13}C NMR (75 MHz, DMSO-d_6); δ 112.34, 122.41, 123.65, 124.87, 124.91, 131.39, 131.43, 131.49, 133.35, 135.45, 144.31, 147.95, 149.86 ppm.

Table 3, entry 10. ^{1}H NMR (300 MHz, DMSO-d_6); δ 7.31 (s, 2H), 7.65–7.69 (m, 2H), 8.39–8.43 (m, 4H), 13.47 (s, 1H) ppm; ^{13}C NMR (75 MHz, DMSO-d_6); δ 124.85, 128.03, 136.69, 148.90, 150.01 ppm.

Table 3, entry 11. ^{1}H NMR (300 MHz, DMSO-d_6); δ 7.31–7.34 (d, 2H), 7.64–7.69 (d, 2H), 8.38–8.45 (m, 4H), 13.32 (s, 1H, NH) ppm; ^{13}C NMR (75 MHz, DMSO-d_6); δ 112.31, 120.21, 122.97, 124.38, 124.88, 128.08, 135.76, 136.74, 144.63, 148.57, 149.59 ppm.

Table 3, entry 12. ^{1}H NMR (300 MHz, DMSO-d_6); δ 7.26–7.31 (m, 2H), 7.67–7.69 (m, 2H), 8.13–8.17 (d, 2H), 8.30–8.33 (d, 2H), 13.21 (brs, 2H, NH, OH) ppm; ^{13}C NMR (75 MHz, DMSO-d_6); δ 123.28, 127.15, 130.81, 132.55, 134.84, 150.96, 167.73 ppm.

Table 3, entry 13. ^{1}H NMR (300 MHz, DMSO-d_6); δ 6.78–6.83 (m, 1H), 6.98–7.01 (m, 1H), 7.19–7.23 (m, 1H), 7.45–7.47 (m, 1H), 7.58–7.62 (m, 4H), 8.12–8.14 (m, 2H), 8.76 (s, 1H), 8.80–8.82 (m, 2H), 9.87 (s, 1H, NH) ppm; ^{13}C NMR (75 MHz, DMSO-d_6); δ 115.65, 117.43, 118.19, 118.18, 121.34, 122.89, 125.45, 126.12, 127.76, 128.58, 128.64, 129.17, 129.46, 130.59, 131.35, 131.63, 135.63, 137.82, 144.59, 145.99, 156.68 ppm.

Table 3, entry 14. ^{1}H NMR (300 MHz, DMSO-d_6); δ 7.29 (s, 2H), 7.66–7.72 (m, 4H), 8.24–7.26 (m, 2H), 13.04 (s, 1H, NH) ppm; ^{13}C NMR (75 MHz, DMSO-d_6); δ 111.93, 119.61, 122.56, 123.48, 128.69, 128.91, 129.53, 129.73, 131.69, 135.14, 135.74, 144.64, 150.89 ppm.

Table 3, entry 15. ^{1}H NMR (300 MHz, DMSO-d_6); δ 7.41 (t, J = 7.6 Hz, 1H), 7.62 (p, J = 4.1 Hz, 4H), 8.01 (d, J = 8.0 Hz, 1H), 8.10–8.13 (m, 3H) ppm; ^{13}C NMR (75 MHz, DMSO-d_6); δ 121.78, 123.64, 125.62, 126.79, 127.93, 129.37, 131.19, 133.66, 135.17, 154.21, 168.54 ppm.

Table 3, entry 16. ^{1}H NMR (300 MHz, DMSO-d_6); δ 7.40–7.43 (m, 1H), 7.46–7.49 (m, 2H), 7.51 (ddd, J = 8.2, 7.1, 1.2 Hz, 1H), 7.94 (dd, J = 8.0, 1.1 Hz, 1H), 8.03–8.05 (m, 2H), 8.08 (d, J = 8.2 Hz, 1H) ppm; ^{13}C NMR (75 MHz, DMSO-d_6); δ 121.79, 123.41, 125.54, 126.67, 128.97, 129.46, 131.99, 135.19, 137.25, 154.28, 166.86 ppm.

Table 3, entry 17. ^{1}H NMR (300 MHz, DMSO-d_6); δ 7.38 (dd, J = 6.0, 3.1 Hz, 2H), 7.57 (d, J = 7.0 Hz, 3H), 7.61–7.64 (m, 1H), 7.81–7.85 (m, 1H), 8.33 (d, J = 6.3 Hz, 2H) ppm; ^{13}C NMR (75 MHz, DMSO-d_6); δ 110.01, 119.16, 123.76, 124.33, 126.31, 126.98, 128.10, 130.78, 141.21, 149.95, 162.26 ppm.

Table 3, entry 18. ^{1}H NMR (300 MHz, DMSO-d_6); δ 7.34–7.36 (m, 2H), 7.52 (d, J = 8.5 Hz, 2H), 7.57–7.59 (m, 1H), 7.75–7.79 (m, 1H), 8.21 (d, J = 8.5 Hz, 2H) ppm; ^{13}C NMR (75 MHz, DMSO-d_6); δ 110.76, 120.27, 124.91, 125.45, 125.89, 129.06, 129.45, 138.12, 142.26, 150.99, 162.30 ppm.

3 Results and discussion

3.1 Structural identification of W–ZnO@NH_2–CBB

As carefully described in the experimental section, W–ZnO nanoparticles were synthesized *via* drop-wise NaOH adding into

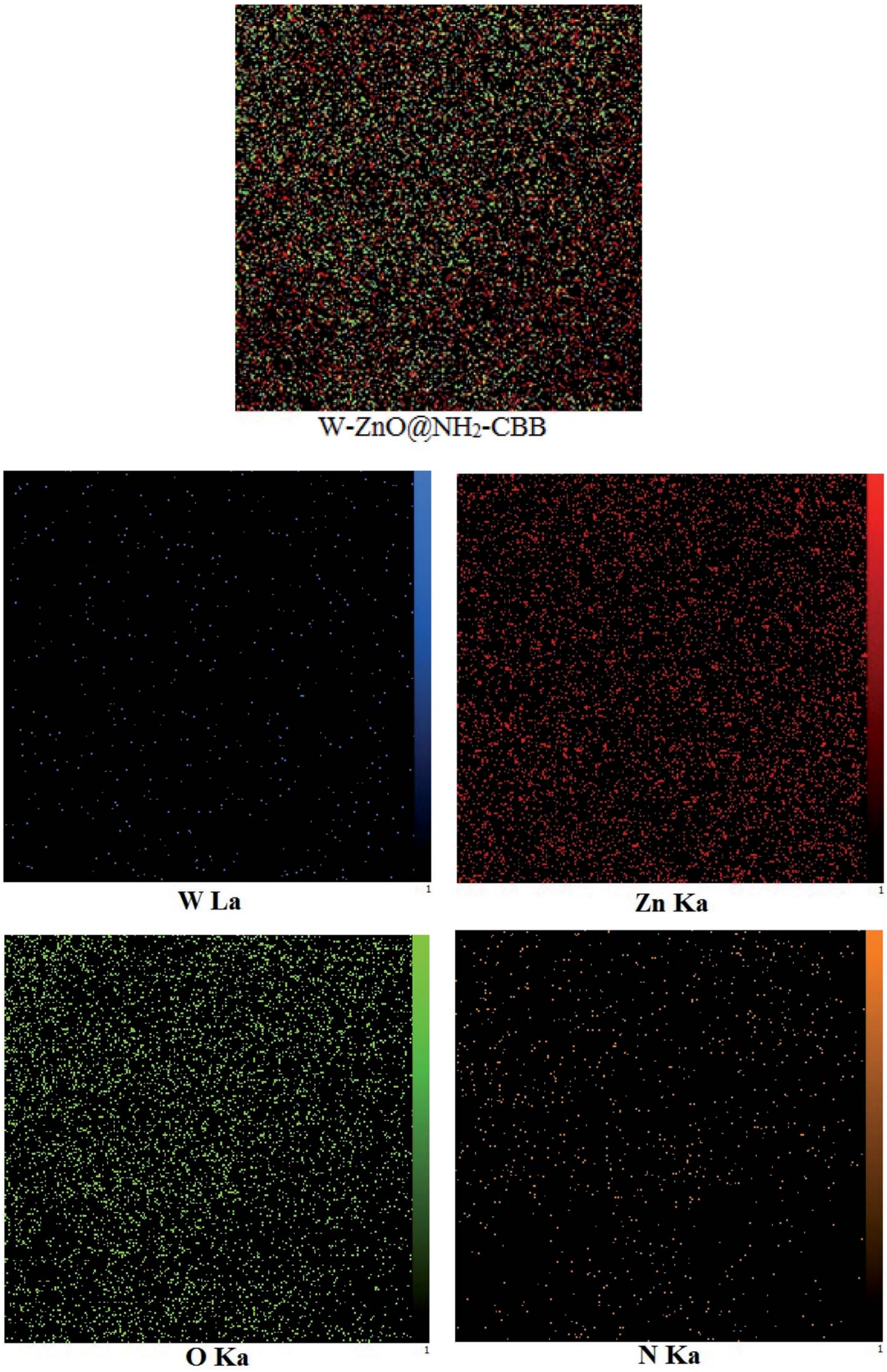

Fig. 3 The FE-SEM map pictures of W–ZnO@NH$_2$–CBB.

a mixture of sodium tungstate and zinc acetate dihydrate in water. Then, the prepared nanoparticles were functionalized with *n*-propylamine and, eventually, CBB was anchored onto the surface of the functionalized W–ZnO@NH$_2$ in THF. The resulting nanomaterial was characterized by means of various techniques including FT-IR, FESEM, TGA, and XRD as follows.

3.1.1 FT-IR. FT-IR spectroscopy was used to recognize the successful loading of CBB onto W–ZnO@NH$_2$ (Fig. 1). In the FT-IR spectrum of CBB (Fig. 1b), the absorption peaks are related to different functional vibrations including aliphatic chains, aromatic rings, –NH, –SO$_3$H and –SO$_3^-$. The broadband between 3600-3100 cm^{-1} is attributed to the O–H vibration of the –SO$_3$H group and NH of the secondary amine.[31] The bands at 2912 and 2850 cm^{-1} correspond to the C–H stretching of the alkyl chains. The C–N stretching vibration of the tertiary amine was approved by the peak at 2233 cm^{-1}. The aromatic skeletal

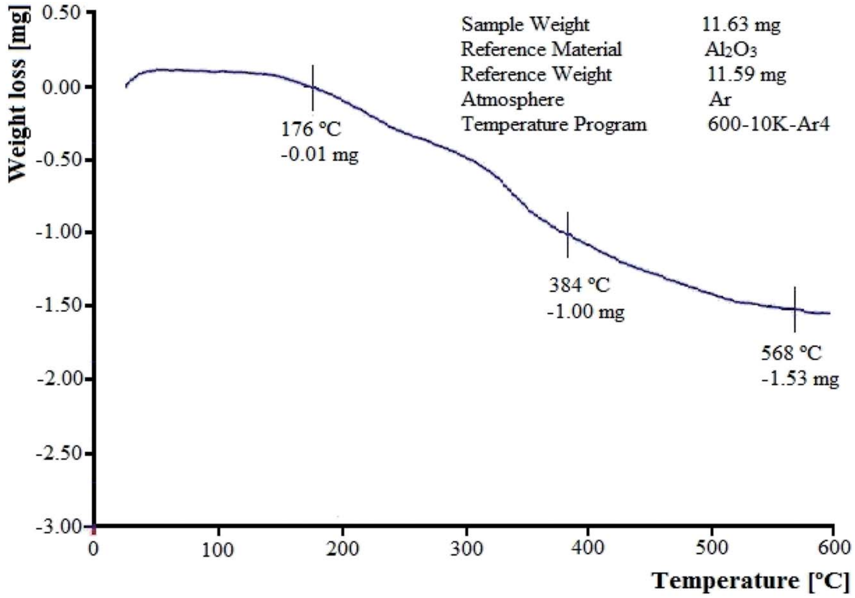

Fig. 4 TGA profile of W–ZnO@NH_2–CBB nanocomposite.

vibrations are observed at 1575 cm^{-1}. The band at 1512 cm^{-1} is due to the bending CH_2 vibration. The band at 1338 cm^{-1} could be due to the stretching of SO_3H group.[31] The peak at 1029 cm^{-1} is due to the S=O stretching in the SO_3H group. The FT-IR spectrum of W–ZnO@NH_2–CBB (Fig. 1c) showed that loading of CBB on W–ZnO@NH_2 has not altered the main IR bands of CBB. In the FT-IR of W–ZnO@NH_2–CBB, two peaks at 673 and 578 cm^{-1} are related to the presence of W–O and Zn–O, respectively.[32,33]

3.1.2 FESEM images. FESEM is a powerful technique to describe the morphological features of the synthesized compounds. FESEM images of W–ZnO@NH_2 and W–ZnO@NH_2–CBB nanoparticles are, respectively, shown in Fig. 2a and b. It is well recognizable that the nanocatalyst particles have a dimension of about 46–54 nm and there is a little agglomeration. Moreover, the FE-SEM map pictures of W–ZnO@NH_2–CBB are also presented to show the distribution of tungsten, zinc, oxygen and nitrogen (Fig. 3). As seen in these pictures, the presence and steady distribution of these elements is well demonstrated in the nanocatalyst particles.

The EDS analysis of W–ZnO showed the W content of about 4.4 at% in the prepared composite, which approves the semi-quantitative amount of 5 mol% WO_3 in the composite based on the amount of used Na_2WO_4. However, less W found in W–ZnO composite than that provided in the precursor solution confirmed that part of the W element would be remained in the mother liquor.[30]

3.1.3 Thermo-gravimetric analysis. TGA curve of W–ZnO@NH_2–CBB nanoparticles at the temperature range of 0 to 600 °C is shown in Fig. 4. The TGA profile describes the thermal

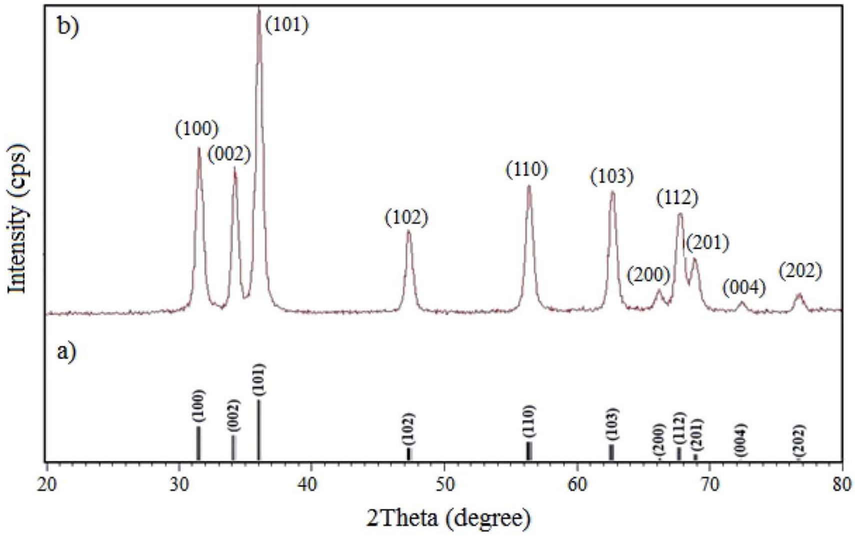

Fig. 5 XRD patterns of (a) simulated standard ZnO and (b) real W–ZnO@NH_2–CBB.

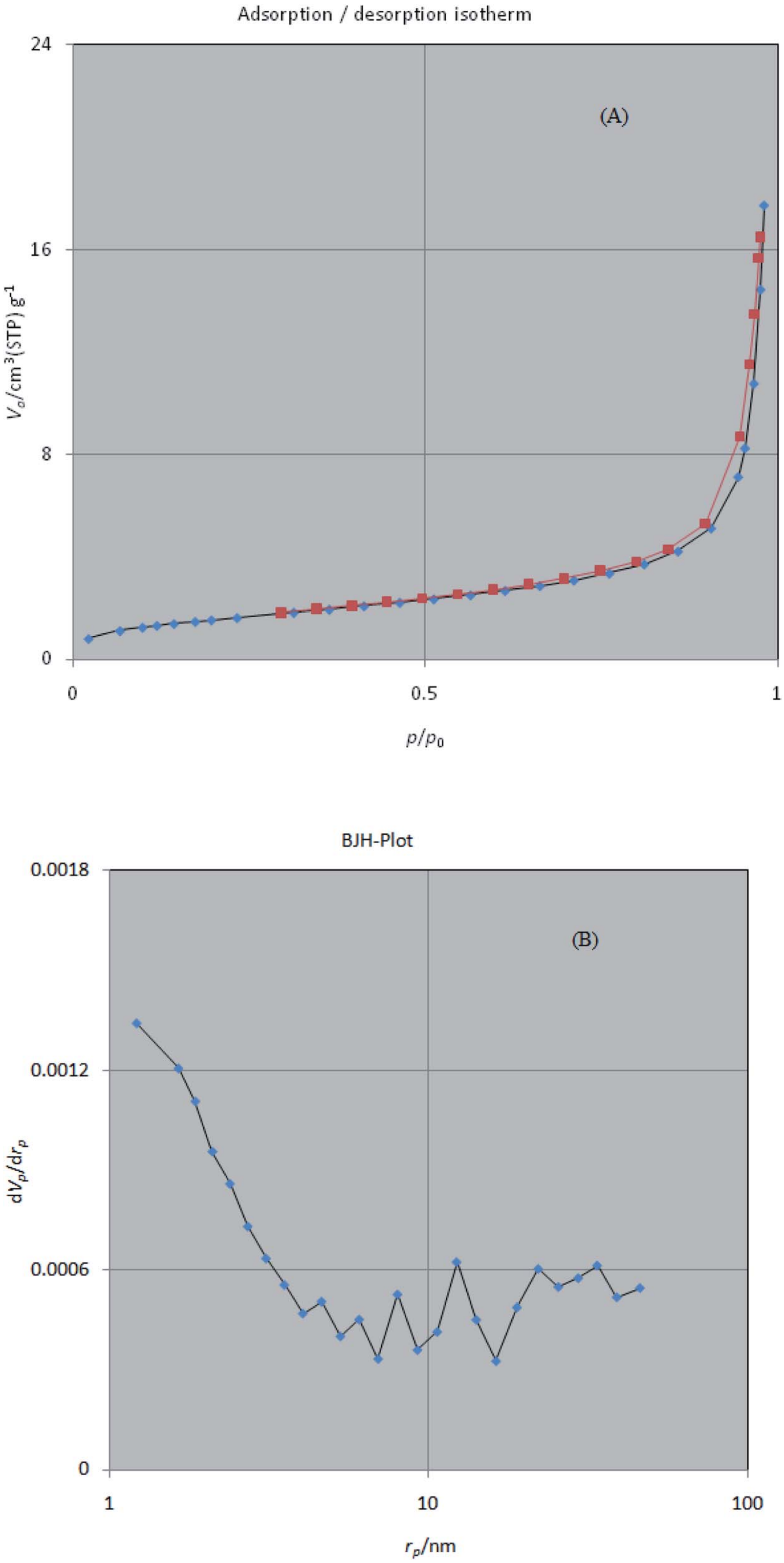

Fig. 6 N_2 adsorption–desorption isotherms (A) and pore size distribution according to the BJH method (B) for W–ZnO nanocomposite.

stability of the sample and the amount of chemical adsorption of the synthesized compound. Initial ascending behavior in the TGA curve of W–ZnO@NH_2–CBB between 22–76 °C can be explained as the consequence of the buoyancy effect of the instrument. This effect has been reported in other studies and it has been stated that the initial increase in weight is due to the

Table 1 Textural properties of pure ZnO and W–ZnO[a]

Sample	S_{BET} ($m^2\ g^{-1}$)	V_{total} ($cm^3\ g^{-1}$)	r_p (nm)
ZnO	10.7	0.134	47.2
W–ZnO	12.4	0.155	29.3

[a] S_{BET}: BET surface area; V_{total}: total pore volume; r_p: average pore diameter.

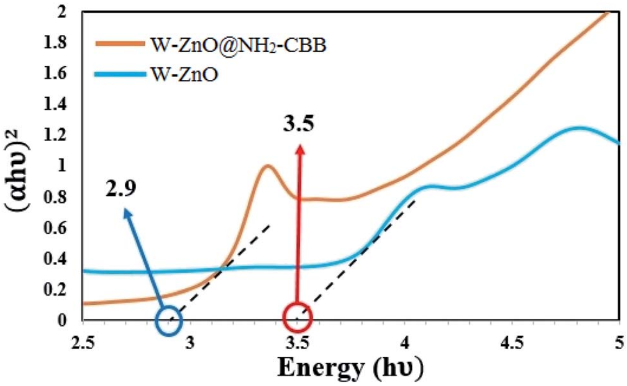

Fig. 7 Optical band-gap analysis of W–ZnO@NH_2–CBB and W–ZnO.

difference in the heat capacity and thermal conductivity of the applied purging gas.[34] The first weight-loss between 176 and 384 °C is due to the loss of COOH groups on CBB.[35] The second weight-loss between 384 °C and 568 °C is assigned to the elimination of *n*-propylamine.

3.1.4 XRD. The XRD patterns of the standard ZnO and W–ZnO@NH_2–CBB nanoparticles are shown in Fig. 5. The sharp peaks at the 2θ of 77.52°, 73.20°, 69.62°, 68.52°, 66.91°, 63.4°, 57.11°, 48.10°, 36.84°, 35.00°and 32.30° are the corresponding peaks of (202), (004), (201), (112), (200), (103), (110), (102), (101), (002) and (100) miller indices, respectively, which agree with the standard XRD pattern of ZnO.[36] The half-value crystallite scale can be calculated by using the XRD data in the Debye–Scherrer formula, which confirmed the value of about 48 nm, in accord with the FESEM analysis. There was no detectable diffraction due to the presence of doped WO_3 in the XRD pattern, which could be attributed to the too low concentration and/or amorphous structure of the dopant.[37,38] However, the existence of W was obviously confirmed by the FESEM map pictures of W–ZnO@NH_2–CBB in Fig. 3.

3.1.5 BET. The surface area and pore distribution of W–ZnO nanocomposite were monitored using nitrogen adsorption–desorption isotherm at 77 K (Fig. 6a). According to previous reports, the specific surface area of W–ZnO is greater than that of pure ZnO, mainly due to the reduction of ZnO crystallite size in the presence of WO_3.[39] However, the increase of surface area is beneficial to the photocatalytic activity of ZnO. The corresponding isotherm exhibited an increase at a relatively low pressure ($P/P_0 < 0.1$), resembling the main characteristics of a porous structure.[40] It seems that W–ZnO nanocomposite obeys a typical type-IV isotherm with a hysteresis loop in the range of $P/P_0 \sim 0.7$–0.9. However, observation of a high adsorption capacity at a relatively high pressure ($P/P_0 > 0.8$) suggests the coexistence of meso- and macro-pores.[41] The pore size distribution of W–ZnO was calculated by the BJH method in the range of 1–100 nm (Fig. 6b). This study indicated a relatively wide distributed pore structure. The textural properties of W–ZnO including the BET surface area, micropore volume, and total pore volume are summarized in Table 1.

3.1.6 Optical band-gap analysis. Optical band-gap analysis was performed to evaluate the band-gap of W–ZnO@NH_2–CBB in comparison with W–ZnO. The optical band-gaps of these two samples were estimated using the Tauc plot based on extrapolation of the linear slope to photon energy (Fig. 7). The calculated band-gap energy of W–ZnO@NH_2–CBB and W–ZnO was found to be 2.9 and 3.5 eV, respectively. This study obviously showed that surface modification and grafting of CBB on the surface of W–ZnO reduced the band-gap 0.6 eV, therefore, increased the photocatalytic efficacy of the heterogeneous catalyst.

3.2 Photocatalytic tests

To study the photocatalytic activity of W–ZnO@NH_2–CBB, the pre-determined amount of benzyl alcohol was reacted with *o*-phenylenediamines in ethanol in the presence of the nanocomposite photocatalyst at room temperature and under the irradiation of an HP-Hg lamp to produce the desired benzimidazole. To define the best conditions for this reaction, we optimized various parameters such as type and amount of photocatalyst, reaction time, irradiation source and ratio of W–ZnO@NH_2 to CBB.

3.2.1 Studying efficacy of different photocatalysts. At first, the effect of various photocatalysts was examined on the reaction efficiency (Fig. 8). This reaction was performed at room temperature in open air. In the presence of photocatalyst and after 2 h, coomassie brilliant blue (CBB) produced the highest yield. The significant high yield% in the presence of CBB confirmed that this organic photosensitizer is the best choice to be functionalized onto W–ZnO@NH_2 nanoparticles. In the following, the model reaction was also carried out in the absence of photocatalyst and in the presence of several other organic and/or inorganic photosensitizers (Fig. 8a and b). As can be seen, W–ZnO@NH_2–CBB showed the best photocatalytic efficiency (95% product after 2 h).

Although our literature survey showed that W (5 mol%) ZnO is revealed the best photocatalytic activity in the photodegradation of some drugs and synthetic colors, however, its photocatalytic activity was compared with 2 and 10 mol% W in W–ZnO. According to Fig. 8b, 2, 5, and 10 mol% W in ZnO gave rise to 26, 41, and 35% yield at the same reaction conditions, respectively. Previous reports show that enhancing WO_3 content suppresses the recombination of the photo-generated electrons and holes.[30,42,43] Therefore, W (5 mol%)ZnO was chosen as the best nanoadsorbent and used to functionalize CBB to attain the target nanophotocatalyst.

3.2.2 Effect of photocatalyst amount and reaction time on the reaction progress. The model reaction was carried out in the

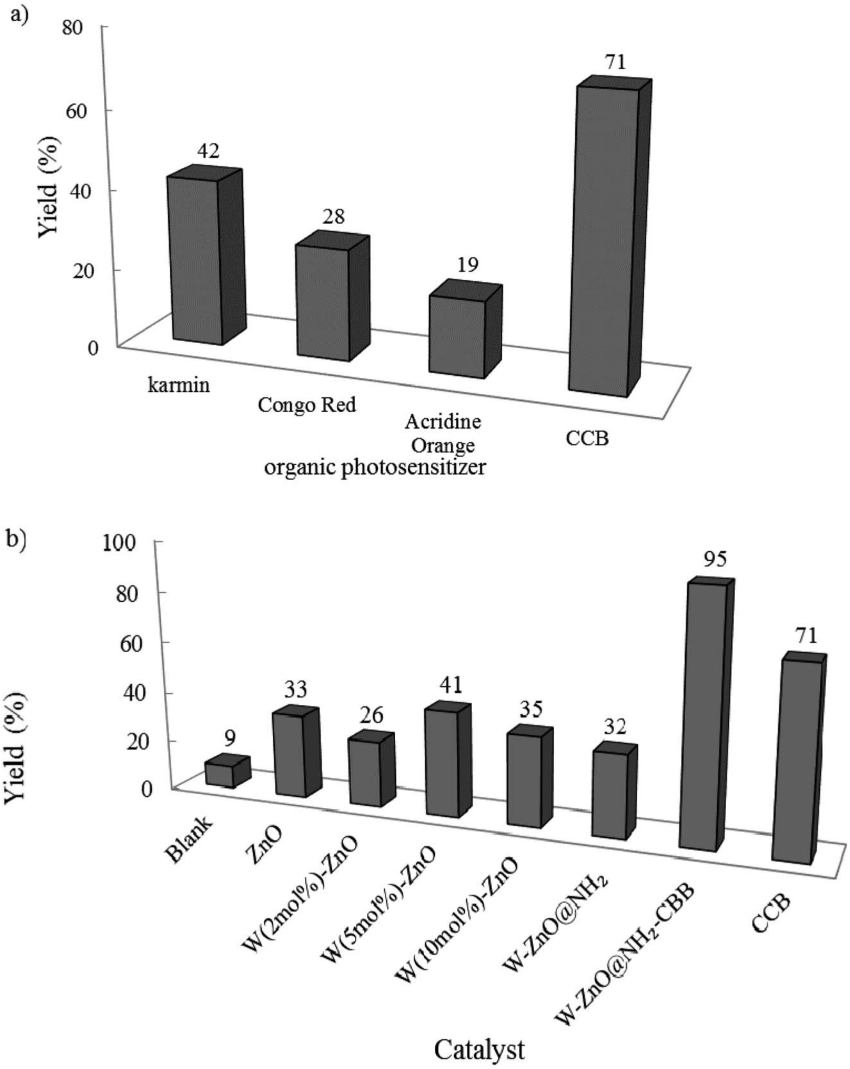

Fig. 8 Effect of different photocatalysts on the reaction progress. Benzyl alcohol and *o*-phenylenediamine selected as the starting materials and reactions were performed under an open atmosphere at room temperature in ethanol (10 mL) using an HP-Hg lamp for 2 h. 0.02 g of photocatalyst was used in all cases.

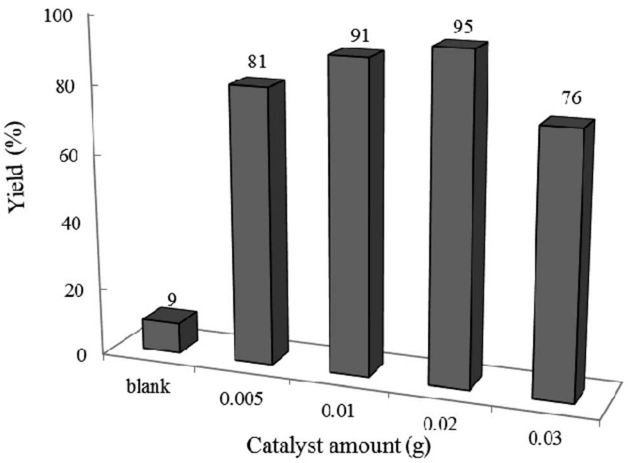

Fig. 9 Effect of photocatalyst amount on the efficiency of condensation reaction of benzyl alcohol with *ortho*-phenylenediamine at 25 °C in ethanol (10 mL) under air and UV-vis irradiation for 2 h.

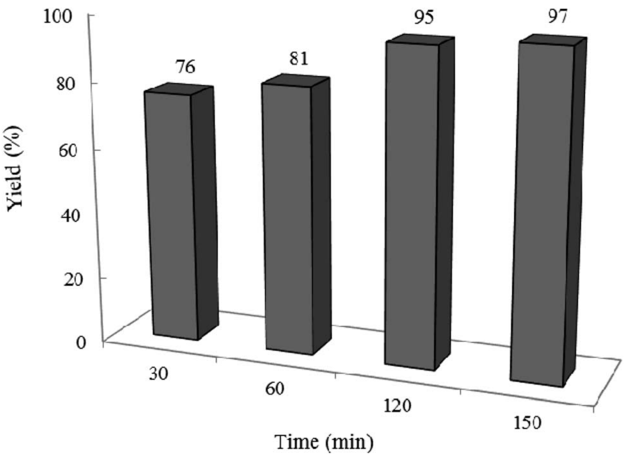

Fig. 10 Effect of reaction time on the yield%. Reaction conditions are similar to that in the caption of Fig. 8. 0.02 g of photocatalyst was used in all cases.

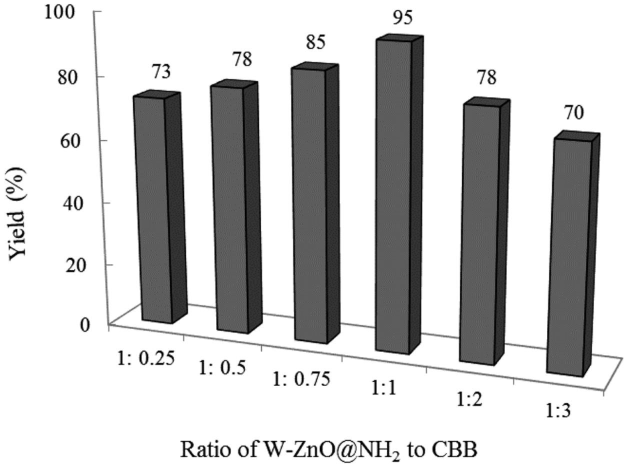

Fig. 11 Effect of W–ZnO@NH$_2$: CBB ratio on the efficacy of condensation reaction. Reaction condition is similar to that in the caption of Fig. 8. Reaction time was 2 h. 0.02 g of photocatalyst was used in all cases.

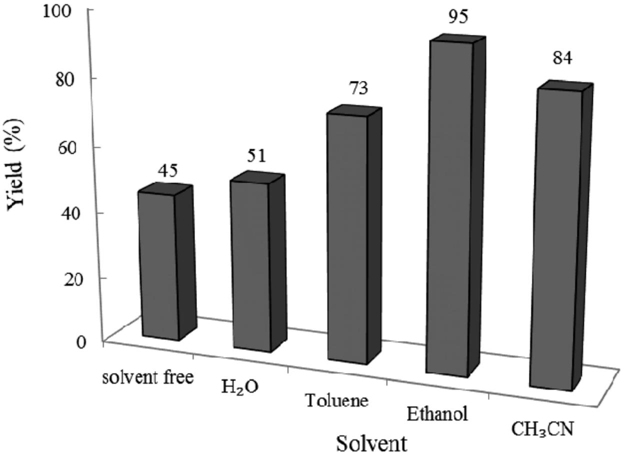

Fig. 12 Effect of solvent on the efficacy of condensation reaction at 25 °C in 10 mL solvent under air and UV-vis irradiation. Reaction time was 2 h. 0.02 g of photocatalyst was used in all cases.

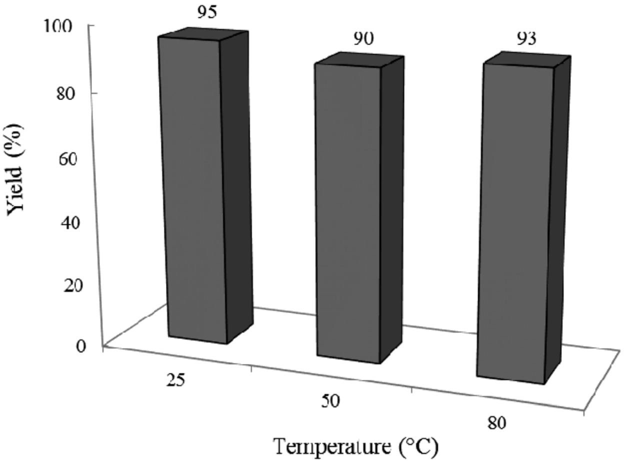

Fig. 13 Effect of temperature on the efficacy of the condensation reaction. Reaction time was 2 h in 10 mL ethanol under air and UV-vis irradiation. 0.02 g of photocatalyst was used in all cases.

absence and presence of W–ZnO@NH$_2$–CBB with different amounts to explore the optimum time and photocatalyst amount required to acquire the maximum yield. The best result was obtained with 0.02 g of photocatalyst after 2 h and neither an increase in the reaction time more than 2 h nor an increase in the amount of photocatalyst greater than 0.02 g affected significantly the reaction efficiency (Fig. 9 and 10). Although there is only a low difference in the yield% (95% compared to 91% in Fig. 9), however, we used the optimum amount of 0.02 photocatalyst in all cases because we realized that the experiments are more repeatable in this case.

3.2.3 Effect of W–ZnO@NH$_2$: CBB ratio on the reaction progress. As expected, the ratio of W–ZnO@NH$_2$ to CBB strongly affected the efficiency of the condensation reaction. Therefore, a model reaction was planned in the presence of 0.02 g of nanocomposite composed of different amounts of CBB ranging from 0.25–3 for W–ZnO@NH$_2$: CBB ratio (Fig. 11). The obtained results revealed that 1 : 1 ratio has been the best and efficiency of the photocatalyst was decreased with further enhancing the CBB amount, maybe due to the enhanced scattering and decreased penetration depth of the incident light.[44,45] Furthermore, decreasing the photocatalyst efficacy with the higher amounts of CBB would be due to masking of W–ZnO surface with this material, which effectively alleviated efficacy of W–ZnO@NH$_2$–CBB.

Table 2 Effect of the light source on the reaction progress[a]

Entry	Light source	Maximum emission lines (nm)	Commercial specification	Photocatalyst amount (g)	Yield (%)
1	HP-Hg	200–450, 530–580	200 W	0.01	91
2	Xenon	820–980	1000 W	0.01	41
3	White LED	400–700	50 W	0.01	29
4	White LED	400–700	20 × 1 W	0.01	25
5	Green LED	500–550	2.5 W	0.01	20
6	Red LED	600–650	2.5 W	0.01	22
7	Sun light	250–1000	—	0.01	15
8	—	—	—	0.01	6

[a] 0.01 g of W–ZnO@NH$_2$–CBB photocatalyst was added to a mixture of benzyl alcohol (1 mmol) and *ortho*-phenylenediamine (0.08 g, 1.2 mmol) in 10 mL ethanol for 2 h.

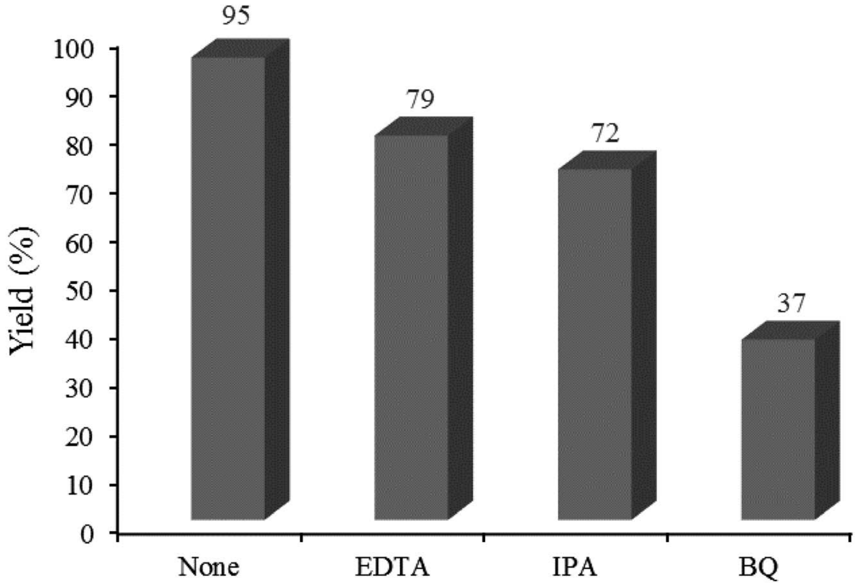

Fig. 14 Effect of some familiar scavengers on the reaction progress under the standard reaction conditions described below Table 2. 0.02 g of photocatalyst was used in all cases.

3.2.4 Effect of irradiation source on the reaction progress. The light source is another influencing factor, which strongly affects the reaction efficiency. The model reaction was exposed to different light irradiations, and the results are given in Table 2. According to the attained results, the best efficiency has been achieved with the HP-Hg lamp. Although, xenon light has a high power and intensity in the spectral region of 820–980 nm, however, it showed low activity and about 41% yield was attained. All performed LEDs provided comparable 20–29% yields. In the case of white LED, enhancing power from 20 to 50 W increased yield% from 25 to 29%, thus, light intensity contributed to the photocatalytic efficacy. For both green and red LEDs, yields are very similar apart from different emission spectrum. It should be noted that although emission intensity is an important parameter, however, the existing literature and our recent results on other multi-component condensation reactions show that these types of LEDs (2.5 W) are typically effective, as will be published soon.[46,47]

3.2.5 Effect of different solvents on the reaction progress. To determine the best solvent for the reaction, we designed the condensation reaction of W–ZnO@NH_2–CBB nanocomposite (0.02 g) as photcatalyst, benzyl alcohol (1 mmol) and *o*-phenylenediamine (1.2 mmol) in the selected solvent (10 mL) at room temperature for 2 h. As can be seen in Fig. 12, ethanol was the best choice between the utilized solvents.

3.2.6 Effect of different temperatures on the reaction progress. In another attempt, the impact of reaction temperature was studied on the standard condensation reaction (Fig. 13). Interestingly, yield% was only a little affected by the reaction temperature, therefore, the temperature of 25 °C was kept as the best for all runs throughout this study.

3.2.7 Studying some hole/electron scavengers. Effect of some familiar hole and electron scavengers is investigated in the current photocatalytic reactions in the presence of W–ZnO@NH_2–CBB (Fig. 14). As documented in the literature, hydroxyl radical, holes and superoxide anion-radical can contribute to the photocatalysis routes. Therefore, a number of familiar scavengers were separately studied in the present photocatalytic reaction. In the presence of isopropyl alcohol (IPA), as a hydroxyl free radical scavenger,[48] yield% was decreased from 95 to 72%. In addition, a large decrease in yield% (95 to 37%) in the presence of *p*-benzoquinone (BQ) revealed that $\cdot O_2^-$ would be involved in the reaction mechanism.[49] Furthermore, ~16% decrease in yield% by the presence of EDTA confirmed that h^+ would also contribute to the photocatalysis reaction.[50] As a result, $OH^\bullet$, $\cdot O_2^-$ and h^+ are expected to be regarded as reactive species in the present photocatalytic reaction.

3.2.8 Synthesis of different benzimidazoles, benzothiazoles and benzoxazoles catalyzed by W–ZnO@NH_2–CBB. In order to determine the scope of this method, some aromatic alcohols bearing electron-withdrawing and electron-donating groups were treated with *o*-phenylenediamine, 2-aminothiophenol and 2-aminophenol to provide the desired benzimidazoles, benzothiazoles and benzoxazoles under the optimum reaction conditions (Table 3). Most of the performed aldehydes provided good to excellent yields in a short period of time. Benzyl alcohols bearing electron withdrawing/releasing substituents successfully generated the desired products with good yields and with superior selectivity. Although most of the electron-rich and electron-poor reagents afforded the desired products in high yields, however, our experiments revealed that benzyl alcohols bearing electron-withdrawing groups react with better efficacy than those bearing electron-donating substituents.

3.2.9 W–ZnO cytotoxicity assay. A preliminary MTT assay was applied to ascertain cytotoxicity of W–ZnO nanoparticles

Table 3 Synthesis of different benzimidazoles, benzothiazoles and benzoxazoles catalyzed by W–ZnO@NH_2–CBB[a]

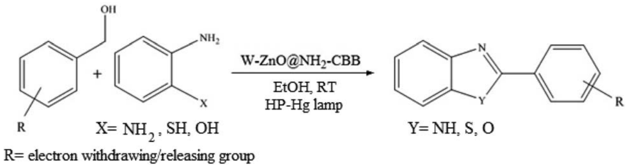

Entry	Benzyl alcohols	*o*-Substituted anilines	Product	Yield (%)	Mp (°C)
1	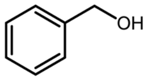	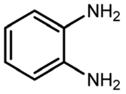	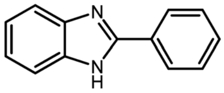	95	290–294
2	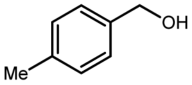	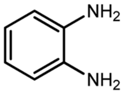	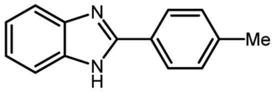	88	263–265
3	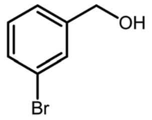	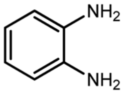	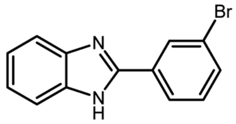	93	284–286
4	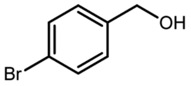	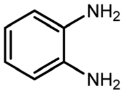	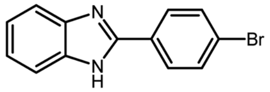	96	291–293
5	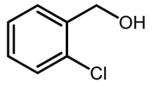	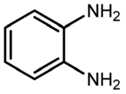	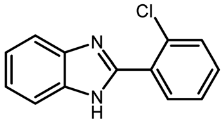	95	228–230
6	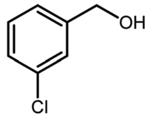	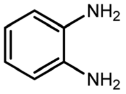	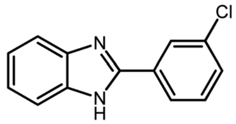	93	253–256
7	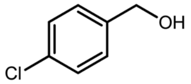	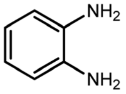	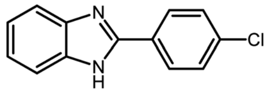	97	289–291
8	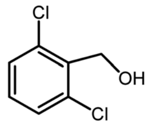	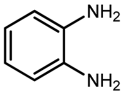	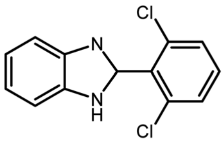	98	272–275
9	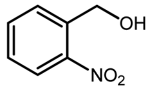	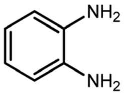	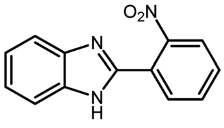	97	212–214
10	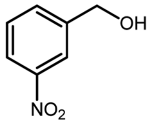	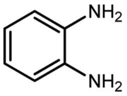	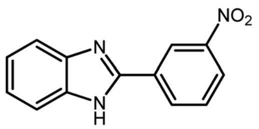	95	310–311
11	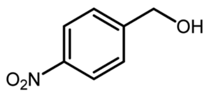	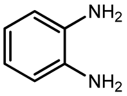	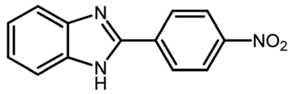	98	309–310
12	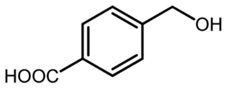	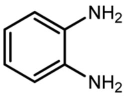	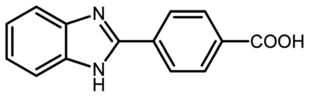	99	>300

Table 3 (*Contd.*)

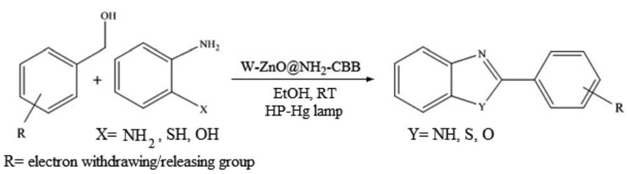

Entry	Benzyl alcohols	*o*-Substituted anilines	Product	Yield (%)	Mp (°C)
13	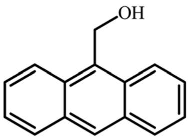	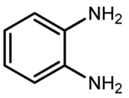	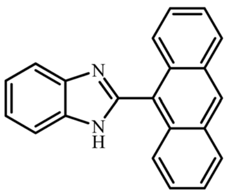	92	>330
14	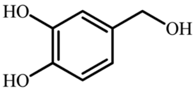	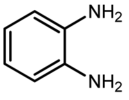	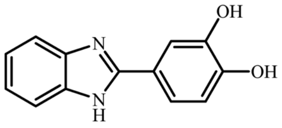	90	269–273
15	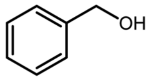	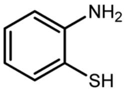	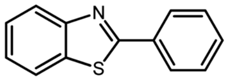	94	110–112
16	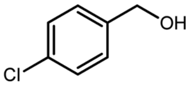	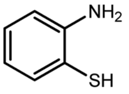	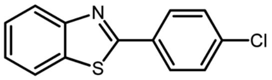	97	114–116
17	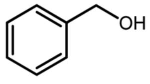	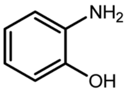	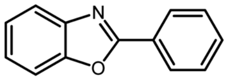	95	201–203
18	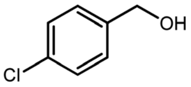	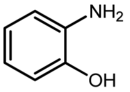	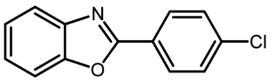	99	209–211

[a] Benzyl alcohols (1 mmol) and substituted anilines (1.2 mmol) were stirred in ethanol (10 mL) under an HP-Hg lamp irradiation for 2 h. 0.02 g of W–ZnO@NH_2–CBB was used as catalyst.

against breast cancer MCF7 cell line. As is well-known, the yellow MTT converts to the formazan purple salt in living cells and a buffer solution of dimethyl sulphoxide can dissolve the solid formazan to a colored form. Then, the absorbance of the colored solution can be determined *via* spectrophotometery at the wavelength of 550 nm. However, the absorption maxima are dependent to the nature of solvent and the cell viability% can be calculated according to the number of the total and viable cells. This experiment showed that the cell viability significantly decreases in the presence of W–ZnO nanoparticles (5–40 μg mL^{-1}) in a dose-dependent fashion after 24 h incubation (Fig. 15). This preliminary study confirmed that the performed nanoparticles affect the cell viability and show cytotoxicity effects on MCF7 cell line.

3.2.10 Comparison of this protocol with the reported similar methods. We compared the gained results for the catalytic activity of W–ZnO@NH_2–CBB with some similar reported catalysts in the synthesis of 2-(*p*-tolyl)-1*H*-benzo[*d*]imidazole in terms of yield%, catalyst amount, reaction time, temperature, solvent and other reaction conditions (Table 4). According to these data, the present method seems to be the best by consideration of the reaction time, catalyst amount, kind of solvent and reaction temperature.

3.2.11 Hot filtration test. A hot filtration test was performed to ensure that the photocatalytic activity originates from the whole W–ZnO@NH_2–CBB and not from the leached fragments. For this purpose, condensation of benzyl alcohol (1 mmol) and *ortho*-phenylenediamine (0.08 g, 1.2 mmol) in ethanol and under the irradiation of an Hg lamp was carried out in the presence of 0.02 g W–ZnO@NH_2–CBB. The obtained yield was 81% after 60 min. Then, toluene was added to dissolve all reagents and products except for the photocatalyst, thus, W–

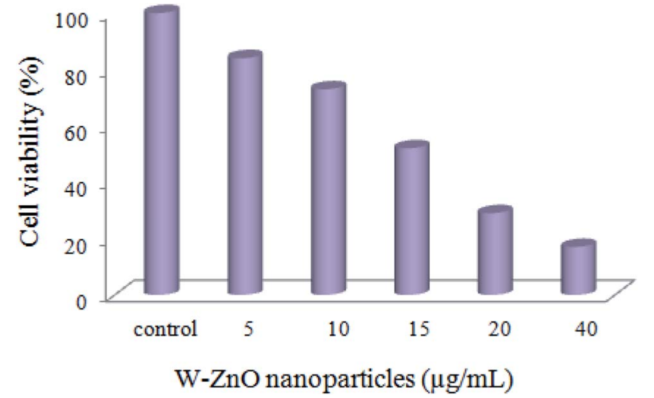

Fig. 15 MTT assay of MCF7 cells exposed to different concentrations of W–ZnO nanoparticles after 24 h.

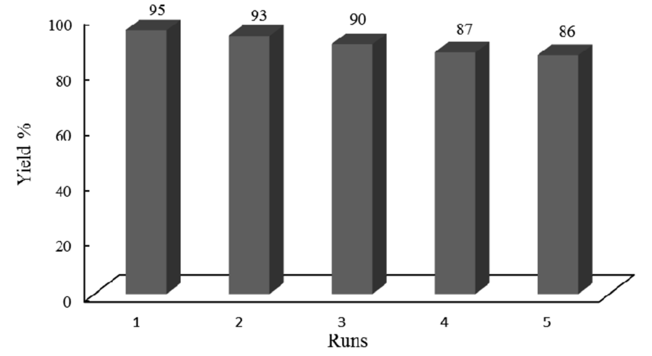

Fig. 16 Studying recyclability of W–ZnO@NH_2–CBB under the optimized reaction conditions. 0.02 g of photocatalyst was used in all cases.

ZnO@NH_2–CBB was easily separated from the reaction mixture. Thereafter, the reaction was continued with the filtrate at the same condition. No significant increase in the yield% of product was reached after another 60 min, proofing that leaching of W–ZnO@NH_2–CBB would not carry out and the photocatalyst is stable, as confirmed by the reusability experiments (Fig. 16).

3.2.12 Recovery and reusability of W–ZnO@NH_2–CBB. Due to the high importance of the recycling and reusing of heterogeneous catalysts in the academic and industrial research, reusability of W–ZnO@NH_2–CBB was studied in the desired condensation reaction. Therefore, after completion of each run, toluene was added and the catalyst was separated from the reaction through a simple filtration. The filtered catalyst was washed with toluene thoroughly and dried at room temperature, then used in the same reaction for five successive runs. The results showed good reusability of W–ZnO@NH_2–CBB (Fig. 16). Furthermore, we compared the XRD of final reused catalyst with that of the fresh one (Fig. 17a and b). The results showed that XRD of the reused W–ZnO@NH_2–CBB after fifth run is almost the same as that of the fresh one and no significant changes can be observed in terms of peak position. To ascertain that W and CBB are maintained in the reused photocatalyst, FT-IR of this material is compared with the fresh one (Fig. 18a and b). As anticipated, the corresponding stretchings due to W and CBB fragments are visible; thus, no significant leaching would occur in the reused photocatalyst. The SEM image of the recycled photocatalyst is also given in Fig. 19. Particles smaller than 50 nanometer in size are still easily recognizable, however, some aggregation is evident in the recycled photocatalyst.

3.2.13 Proposed reaction pathway. A plausible reaction pathway is outlined for the synthesis of benzimidazole derivatives in Scheme 2. According to this route, initially W–ZnO@NH_2–CBB activates the dehydrogenative oxidation of benzyl alcohol with air in the presence of light to form the corresponding benzaldehyde (1). The *in situ* generated benzaldehyde reacts with *o*-phenylenediamine to produce an imine intermediate (2), which is accompanied by the release of a water molecule. Subsequently, the imine intermediate that is in equilibrium with the corresponding dihydrobenzimidazole (3), can be catalytically dehydrogenated with air to generate the desired final benzimidazole product. Although previous reports[56] strongly commented that conversion of imine intermediate to the corresponding benzimidazole would involve generation of intermediate (3), however, it seems that the protodeauration of imine intermediate (2) should be very fast because we failed to detect it by NMR. In addition, performing this reaction in N_2 atmosphere, led to a significant decrease in the yield% from 95 to

Table 4 Comparison of the catalytic activity of W–ZnO@NH_2–CBB with some reported catalysts in the synthesis of 2-(*p*-tolyl)-1*H*-benzo[*d*]imidazole

Catalyst	Time (h)	Temp. (°C)	Solvent	Yield (%)	Ref.
W–ZnO@NH_2–CBB (0.02 g)	2	Room temperature, UV-vis condition	Ethanol (10 mL)	95	This work
Ir/TiO_2 (2.0 wt%)	18	120 °C under Ar	—	87	51
TiO_2/AA/Co (0.06 mol%)	3	70 °C under air, visible-light	—	83	52
Co(II)–TD@TiO_2 (2 mol%)	3	80 °C, visible-light, O_2 (5–7 mL min^{-1})	—	79	53
$Mo_{72}V_{30}$ (0.05 mol%) in combination with NHPI (10 mol%)	6	70 °C, under O_2 (1 atm)	EtOAc (2 mL)	89	54
$[MIMPs]^+$ Cl^- (20 mol%) in combination with TEMPO (5 mol%) and $NaNO_2$ (8 mol%)	10	At 2 steps: $T_1 = 45$ °C, $T_2 = 55$ °C, under O_2	CH_3CN/H_2O (2 mL/2 mL)	94	55

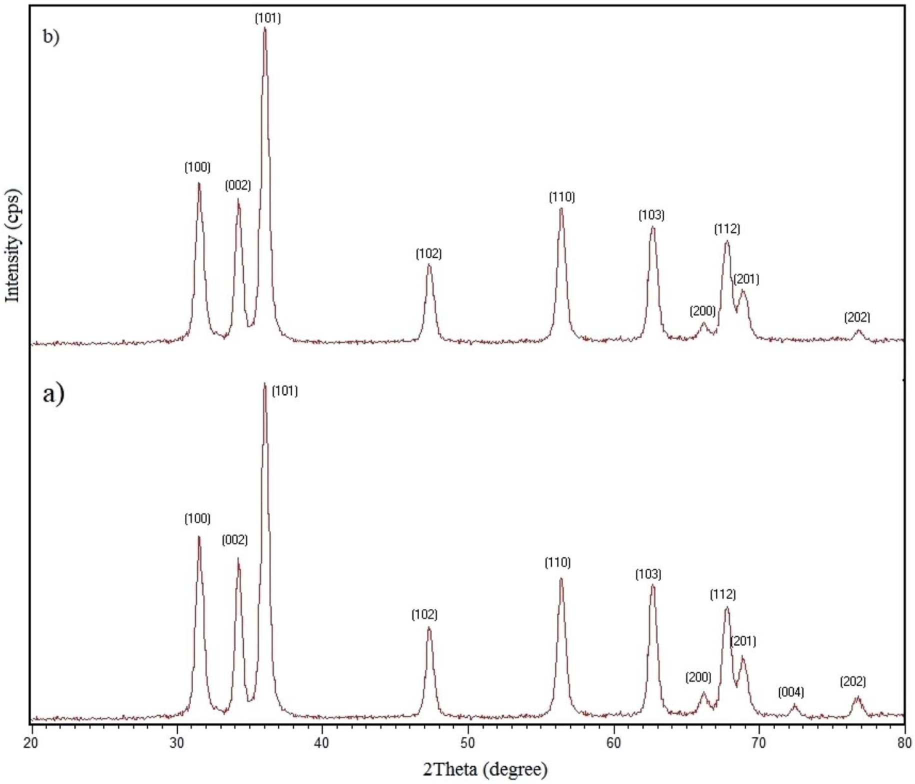

Fig. 17 XRD patterns of the fresh (a) and final reused photocatalyst (b).

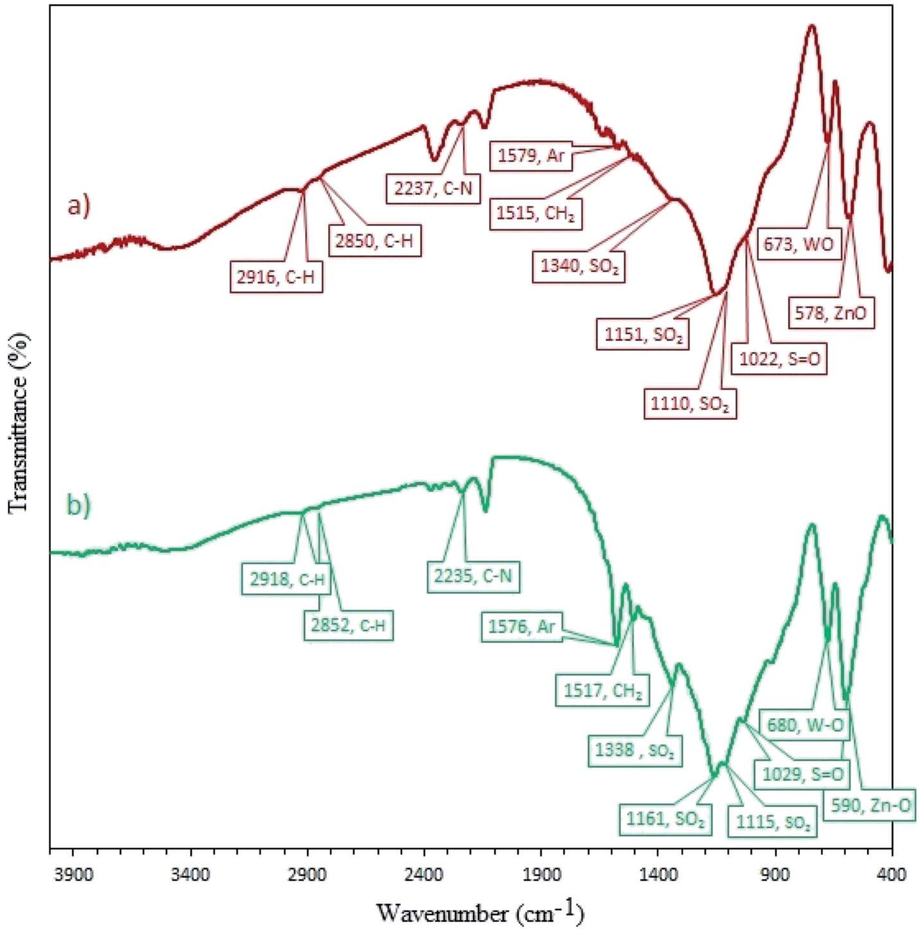

Fig. 18 FT-IR spectra of the fresh (a) and final reused photocatalyst (b).

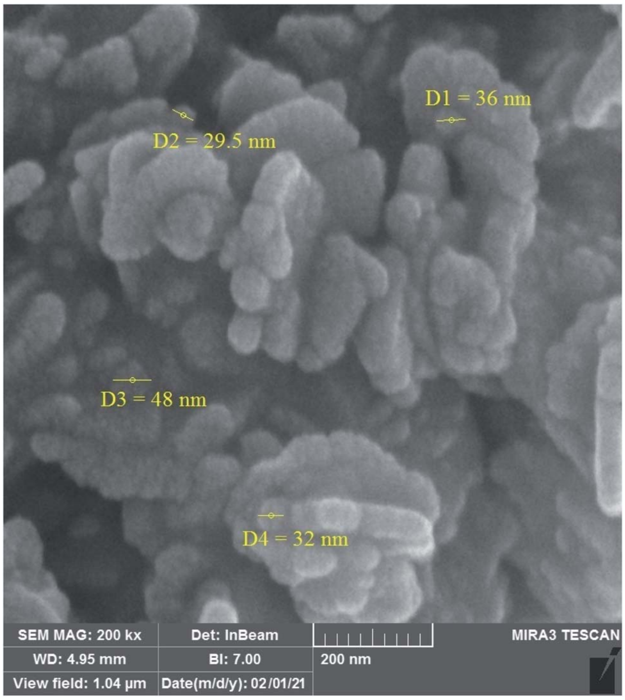

Fig. 19 FESEM images of the final reused photocatalyst.

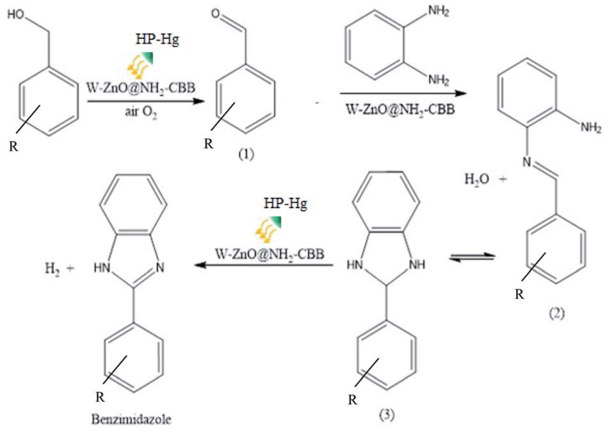

Scheme 2 A suggested mechanism for the synthesis of 2-substituted benzimidazoles catalyzed by W–ZnO@NH$_2$–CBB.

37%. This finding clearly confirmed the distinct role of oxygen in the reaction progress.

4 Conclusion

In conclusion, we introduced a green heterogeneous and reusable nanophotocatalyst based on W–ZnO@NH$_2$ modified by coomassie brilliant blue (CBB) for the one-pot multi-component photocatalytic synthesis of benzimidazoles, benzothiazoles and benzoxazoles in ethanol. The novel photocatalyst was characterized by XRD, FT-IR, TGA and SEM. Some preliminary mechanistic studies demonstrated that the reaction occurs mainly *via* a radical mechanism and reactive species such as $\cdot O_2^-$, $OH^\bullet$ and h^+ would be involved in the photocatalytic process. Stability and reusability studies also confirmed that W–ZnO@NH$_2$–CBB is a stable and reproducible nanophotocatalyst. This methodology suggests various advantages, including good to excellent yield, short reaction time, excellent recovery and reusability of the photocatalyst without significant loss of activity. In addition, no need to use any specific oxidant and the protocol can be expanded to a wide range of benzyl alcohols. Finally, a preliminary MTT assay confirmed that W–ZnO nanoparticles show a significant cytotoxicity against the MCF7 breast cell line.

Conflicts of interest

There are no conflicts to declare.

Acknowledgements

The authors/creators would like to acknowledge the financial support of Ministry of Science, Research and Technology for this project under grant number 12-99-02-000029. Also, the work has been supported by Hakim Sabzevari University. This investigation was approved by Xi'an Central Hospital animal ethical committee, approved no. XASZX210414.

References

1 S. K. Sahoo, *Renewable Sustainable Energy Rev.*, 2016, **59**, 927–939.
2 M. Zhu, Z. Sun, M. Fujitsuka and T. Majima, *Angew. Chem., Int. Ed.*, 2018, **57**, 2160–2164.
3 E. Parvizi, R. Tayebee, E. Koushki, M. F. Abdizadeh, B. Maleki, P. Audebert and L. Galmiche, *RSC Adv.*, 2019, **9**, 23818–23831.
4 S. Shanmugam, S. Xu, N. N. M. Adnan and C. Boyer, *Macromolecules*, 2018, **51**, 779–790.
5 Z. Li, H. Song, R. Guo, M. Zuo, C. Hou, S. Sun, X. He, Z. Sun and W. Chu, *Green Chem.*, 2019, **21**, 3602–3605.
6 L. Zhang and M. Jaroniec, *Appl. Surf. Sci.*, 2018, **430**, 2–17.
7 S. Li, Q. Liang, S. A. H. Ahmed and J. Zhang, *Food Anal. Methods*, 2020, 1–8.
8 C. Tejada-Casado, M. Hernández-Mesa, M. del Olmo-Iruela and A. M. García-Campaña, *Talanta*, 2016, **161**, 8–14.
9 A. Bello, A. Uzairu and G. Shallangwa, *J. Mater. Environ. Sci.*, 2019, **10**, 1–14.
10 S. Saini, N. Dhiman, A. Mittal and G. Kumar, *J. Drug Delivery Ther.*, 2016, **6**, 100–102.
11 M. Shahnaz, P. Kaur, J. Parkash and D. Parsad, *J. Drug Delivery Ther.*, 2018, **8**, 460–464.
12 M. Hossain and A. K. Nanda, *Science*, 2018, **6**, 83–94.
13 H. P. Vemana, L. Barasa, N. Surubhotla, J. Kong, S. S. Ha, C. Palaguachi, J. L. Croft, S. Yoganathan and V. V. Dukhande, *FASEB J.*, 2019, **33**, 618–646.
14 P. Flores-Carrillo, J. M. Velázquez-López, R. Aguayo-Ortiz, A. Hernández-Campos, P. J. Trejo-Soto, L. Yépez-Mulia and R. Castillo, *Eur. J. Med. Chem.*, 2017, **137**, 211–220.
15 A. K. Chaturvedi, A. K. Verma, J. P. Thakur, S. Roy, S. B. Tripathi, B. S. Kumar, S. Khwaja, N. K. Sachan,

A. Sharma and D. Chanda, *Bioorg. Med. Chem.*, 2018, **26**, 4551–4559.

16 S. N. A. Bukhari, G. Lauro, I. Jantan, C. Fei Chee, M. W. Amjad, G. Bifulco, H. Sher, I. Abdullah and N. A. Rahman, *Future Med. Chem.*, 2016, **8**, 1953–1967.

17 M. S. Vasava, M. N. Bhoi, S. K. Rathwa, D. J. Jethava, P. T. Acharya, D. B. Patel and H. D. Patel, *Mini-Rev. Med. Chem.*, 2020, **20**, 532–565.

18 J. Sharma, P. K. Soni, R. Bansal and A. K. Halve, *Curr. Org. Chem.*, 2018, **22**, 2280–2299.

19 X. Wen, J. El Bakali, R. Deprez-Poulain and B. Deprez, *Tetrahedron Lett.*, 2012, **53**, 2440–2443.

20 K. R. Al-Jorani, A. J. K. Atia, S. J. Lafta, R. I. Al-Bayti, S. A. Kadhem and S. M. Baqer, *J. Pharm. Sci. Res.*, 2019, **11**, 1195–1203.

21 C. Rathod, R. Rajurkar and S. Thonte, *Indo Am. J. Pharm. Res.*, 2013, **3**, 2323–2329.

22 K. D. Parghi and R. V. Jayaram, *Catal. Commun.*, 2010, **11**, 1205–1210.

23 S. Das, S. Mallick and S. De Sarkar, *The J. Org. Chem.*, 2019, **84**, 12111–12119.

24 A. Sajjadi and R. Mohammadi, *J. Med. Chem.*, 2019, **2**, 55–58.

25 M. Bharathi, S. Indira, G. Vinoth and K. S. Bharathi, *J. Porous Mater.*, 2019, **26**, 1377–1390.

26 A. Nozarie, *Chem. Methodol.*, 2019, **3**, 768–776.

27 S. Sajjadifar, I. Amini, H. Jabbari, O. Pouralimardan, M. Hossein Fekri and K. Pal, *Eurasian Chem. Commun.*, 2019, **1**, 191–192.

28 K. Wada, H. Yu and Q. Feng, *Chin. Chem. Lett.*, 2020, **31**, 605–608.

29 K. B. Dhopte, R. S. Zambare, A. V. Patwardhan and P. R. Nemade, *RSC Adv.*, 2016, **6**, 8164–8172.

30 J. Xie, Z. Zhou, Y. Lian, Y. Hao, X. Liu, M. Li and Y. Wei, *Ceram. Int.*, 2014, **40**, 12519–12524.

31 M. Maity, S. Dolui and N. C. Maiti, *Phys. Chem. Chem. Phys.*, 2015, **17**, 31216–31227.

32 R. Tayebee, M. Fattahi Abdizadeh, M. Mohammadpour Amini, N. Mollania, Z. Jalili and H. Akbarzadeh, *Int. J. Nano Dimens.*, 2017, **8**, 365–372.

33 S. Bai, K. Zhang, L. Wang, J. Sun, R. Luo, D. Li and A. Chen, *J. Mater. Chem.*, 2014, **2**, 7927–7934.

34 K. S. Babu, A. R. Reddy, C. Sujatha, K. V. Reddy and A. Mallika, *J. Adv. Ceram.*, 2013, **2**, 260–265.

35 H. Alinezhad, M. Tarahomi, B. Maleki and A. Amiri, *Appl. Organomet. Chem.*, 2019, **33**, e4661.

36 S. D. Lee, S. H. Nam, M. H. Kim and J. H. Boo, *Phys. Procedia*, 2012, **32**, 320–326.

37 F. Shirini, M. Abedini, S. Zamani and H. F. Moafi, *J. Nanostruct. Chem.*, 2015, **5**, 123–130.

38 A. Faudoa-Arzate, A. Arteaga-Durán, R. Saenz-Hernández, M. Botello-Zubiate, P. Realyvazquez-Guevara and J. Matutes-Aquino, *Materials*, 2017, **10**, 200.

39 L. Jing, Z. Xu, X. Sun, J. Shang and W. Cai, *Appl. Surf. Sci.*, 2001, **180**, 308–314.

40 M. Humayun, A. Zada, Z. Li, M. Xie, X. Zhang, Y. Qu, F. Raziq and L. Jing, *Appl. Catal., B*, 2016, **180**, 219–226.

41 F. Narenji-Sani, R. Tayebee and M. Chahkandi, *ACS Omega*, 2020, **5**, 9999–10010.

42 K. Tennakone, O. Ileperuma, J. Bandara and W. Kiridena, *Semicond. Sci. Technol.*, 1992, **7**, 423.

43 T. López-León, J. L. Ortega-Vinuesa, D. Bastos-González and A. Elaïssari, *J. Phys. Chem. B*, 2006, **110**, 4629–4636.

44 M. Hoque and M. I. Guzman, *Materials*, 2018, **11**, 1990.

45 P. Johne and H. Kisch, *J. Photochem. Photobiol., A*, 1997, **111**, 223–228.

46 A. K. Sharma, J. Tiwari, D. Jaiswal, S. Singh, J. Singh and J. Singh, *Curr. Organocatal.*, 2019, **6**, 222–230.

47 B. Li, R. Tayebee, E. Esmaeili, M. S. Namaghi and B. Maleki, *RSC Adv.*, 2020, **10**, 40725–40738.

48 R. K. Sharma, B. Arora, S. Sharma, S. Dutta, A. Sharma, S. Yadav and K. Solanki, *Mater. Chem. Front.*, 2020, **4**, 605–620.

49 Z. Yin, M. Han, Z. Hu, L. Feng, Y. Liu, Z. Du and L. Zhang, *Chem. Eng. J.*, 2020, **390**, 124532.

50 X. Zheng, J. Yuan, J. Shen, J. Liang, J. Che, B. Tang, G. He and H. Chen, *J. Mater. Sci.: Mater. Electron.*, 2019, **30**, 5986–5994.

51 K. Tateyama, K. Wada, H. Miura, S. Hosokawa, R. Abe and M. Inoue, *Catal. Sci. Technol.*, 2016, **6**, 1677–1684.

52 F. Feizpour, M. Jafarpour and A. Rezaeifard, *Catal. Lett.*, 2018, **148**, 30–40.

53 A. Eskandari, M. Jafarpour, A. Rezaeifard and M. Salimi, *New J. Chem.*, 2018, **42**, 6449–6456.

54 A. Khoshyan, M. Pourtahmasb, F. Feizpour, M. Jafarpour and A. Rezaeifard, *Appl. Organomet. Chem.*, 2019, **33**, e4638.

55 Z. Geng, H.-y. Zhang, G. Yin, Y. Zhang and J. Zhao, *J. Chem. Res.*, 2020, **44**, 557–565.

56 M. A. Tzani, C. Gabriel and I. N. Lykakis, *Nanomaterials*, 2020, **10**, 2405.